de Broglie wave-front curvature induced by electric-field gradients and its effect on precision measurements with an atom interferometer

Ivan Hromada,[1] Raisa Trubko,[2] William F. Holmgren,[1] Maxwell D. Gregoire,[1] and Alexander D. Cronin[1,2,*]
[1]*Department of Physics, University of Arizona, Tucson, Arizona 85721, USA*
[2]*College of Optical Sciences, University of Arizona, Tucson, Arizona 85721, USA*
(Received 4 December 2013; published 10 March 2014)

To improve precision measurements made with atom interferometers, the effect of de Broglie wave-front curvature induced by a lens inside an atom interferometer is experimentally demonstrated and theoretically analyzed. Electrostatic lenses shift, magnify, and distort atom interference fringes, which modifies the phase and the contrast of the interference signals. Informed by these observations, an improved method is presented for analyzing measurements of atomic beam velocity distributions using phase choppers [W. F. Holmgren, I. Hromada, C. E. Klauss, and A. D. Cronin, New J. Phys. **13**, 115007 (2011)].

DOI: 10.1103/PhysRevA.89.033612 PACS number(s): 03.75.Be, 37.25.+k, 03.75.Dg

I. INTRODUCTION

Atom interferometry is well established as a precision measurement technology with applications in fields such as inertial sensing [1–3], measurements of fundamental quantities [4–6], measurements of atomic properties [7–12], and studies of quantum phenomena such as decoherence [13–16] and geometric phases [17–19]. For reviews of optics and interferometry with neutral atoms and molecules, see [20–22]. Improvements in the precision of these measurements can result from new atom optics techniques to prepare, manipulate, and monitor the atomic de Broglie waves used in atom interferometers. For example, more accurate methods to measure the velocity distribution of the atoms that contribute to interference fringes would help refine measurements of atomic polarizability made with atom interferometers [7–10].

A promising method to measure the velocity distribution of atoms in an atom interferometer utilizes two phase choppers [23] to induce velocity-dependent contrast-loss spectra for atomic fringes. Similar to experiments with mechanical choppers, the result depends on the time of flight between two choppers. However, instead of blocking atomic beam flux, each phase chopper shifts the phase of atomic interference fringes. Two phase choppers pulsing at frequency ν can cause modulations in fringe contrast (as opposed to flux) as a function of frequency, with contrast maxima occurring near $\nu = n v_0/(2L)$, where v_0 is the most probable velocity of the atoms, n is an integer, and L is the distance between phase choppers. We implemented phase choppers by using electric-field gradients to cause differential phase shifts for atomic de Broglie waves because such phase choppers are compact, can be pulsed at audio frequencies, and do not require any moving parts. Our measurements of $v_0 = 1975.3 \pm 1.0$ m/s presented in Sec. VIII of this paper demonstrate a precision of 0.05% using phase choppers made with electric-field gradients.

However, in addition to shifting the phase of atomic interference fringes, we have found that electric-field gradients also magnify and distort the fringes. In Sec. II we show that fringe magnification is inevitable when using electric-field gradients. Fringe magnification is a problem because it changes the observed contrast as a function of chopper frequency and thus influences our measurements of atom beam velocity. Magnification due to de Broglie wave-front curvature induced by phase choppers can cause systematic errors as large as 0.2% in our measurements of velocity, which can lead to 0.4% errors in measurements of atomic polarizability.

To study how de Broglie wave-front curvature affects atom interference fringes, we developed the analogy that phase choppers act like lenses for atomic de Broglie waves. We used an experiment sketched in Fig. 1 to demonstrate how contrast changes and phase shifts caused by a lens can be related to the focal length, spherical aberration, and location of the atom lens as well as several other parameters such as the locations of the nanogratings, the sizes of the collimating slits, and the size of the detector. Lenses for neutral atoms have been made previously by several methods such as using magnetic fields [24–27], electric fields [28–30], zone plates [31,32], and standing waves of radiation [33–35]. Historically, such lenses have been used for atom microscopes [36,37] and for controlling the deposition of atoms on surfaces [38–40]. In this paper we concentrate on how lenses inside an atom interferometer modify interference fringes.

II. WHY FOCUSING IS UNAVOIDABLE

First, we discuss the following question: Can electrodes be fabricated with shapes that produce zero focusing, but still cause deflection of neutral atoms? If we could design a prism for atom waves, then a more ideal phase chopper could be constructed and some of the more complicated analysis presented in this paper could be avoided. However, in this section we conclude that focusing is unavoidable if we use static electric fields from electrodes that are invariant under translation in the y direction. We have chosen symmetry under y translation as a constraint because the y direction is parallel to the nanograting bars and the long axis (height) of the collimating slits and we want the same phase shift ϕ across the height of the atom beam.

We pose this question mathematically by asking if there exists a vector field $\mathbf{E}(x,z)$ that makes nonzero phase shift for atom interference fringes,

$$\phi = \left(\frac{\alpha s}{2\hbar v}\right)\frac{d}{dx}\int \mathbf{E}^2 dz \neq 0, \tag{1}$$

*cronin@physics.arizona.edu

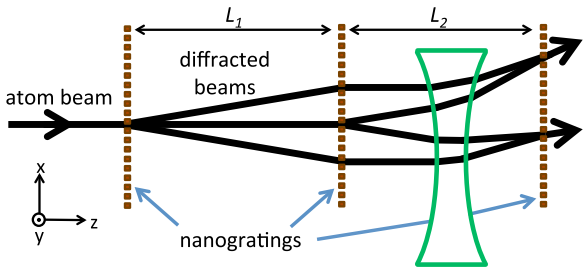

FIG. 1. (Color online) Schematic of a lens for atoms in an atom interferometer. Atoms propagate in the z direction and diffract from nanogratings separated by distances L_1 and L_2. To study how the lens shifts, magnifies, and distorts atomic de Broglie wave interference fringes, we vary L_2 (Sec. V) and translate the lens in the x direction (Sec. VI). $\hat{y}$ points out of the page.

but zero gradient in the phase shift for atom interference fringes,

$$\frac{d\phi}{dx} = \left(\frac{\alpha s}{2\hbar v}\right)\frac{d^2}{dx^2}\int \mathbf{E}^2 dz = 0, \tag{2}$$

where α is the atomic polarizability, s is the separation between paths in the atom interferometer, $\hbar$ is Planck's constant divided by 2π, v is atomic velocity, z is distance along the direction of the incident atom beam, and x is distance transverse to the atom beam (see Fig. 1). For completeness, the phase shift for atomic de Broglie waves passing along one path through an electric field is given by $\Phi = \alpha/(2\hbar v)\int \mathbf{E}^2 dz$ and $\phi = (d\Phi/dx)s$.

We can rewrite Eq. (2) to be

$$\frac{d\phi}{dx} = \left(\frac{\alpha s}{\hbar v}\right)\int\left[\left(\frac{d}{dx}\mathbf{E}\right)^2 + \mathbf{E}\frac{d^2}{dx^2}\mathbf{E}\right]dz. \tag{3}$$

Then, since $\nabla^2\mathbf{E} = 0$, for y-invariant fields we know that $\frac{d^2}{dx^2}\mathbf{E} = -\frac{d^2}{dz^2}\mathbf{E}$. Thus, we can replace the second term in Eq. (3) with $-\mathbf{E}\frac{d^2}{dz^2}\mathbf{E}$ and integrate by parts to show

$$\frac{d\phi}{dx} = \left(\frac{\alpha s}{\hbar v}\right)\int\left[\left(\frac{d}{dx}\mathbf{E}\right)^2 + \left(\frac{d}{dz}\mathbf{E}\right)^2\right]dz. \tag{4}$$

This expression for the focusing power is positive definite. Thus, Eq. (4) shows that focusing power is nonzero if there is any gradient in the electric field, as there must be in order to cause a deflection. Equations (2) and (1) cannot be simultaneously satisfied by an electric field $\mathbf{E}(x,z)$. This proves that de Broglie wave focusing is inevitable when using electric-field gradients to cause fringe phase shifts. Therefore, we are motivated to include the effect of focusing in our analysis of phase choppers. We begin by describing phase choppers as lenses in the following sections.

III. ELECTROSTATIC LENS CONSTRUCTION

We built electrostatic lenses for atoms using two different electrode geometries, referred to here as Lens A and Lens B. Lens A is made from a charged cylinder near a grounded plane. Lens B is made from two parallel cylinders with equal diameters held at opposite voltages where the plane of symmetry between the cylinders remains at zero potential. Each assembly has a gap between the electrodes where atoms pass through inhomogeneous electric fields. Since the lenses work by virtue of polarizable atoms interacting with electric-field gradients, the lenses can be turned on by applying a voltage and turned off by grounding the electrodes. Table I summarizes the electrode dimensions and resulting focal lengths in our experiment.

TABLE I. Electrostatic lens dimensions and operating voltages. Focal lengths (f) are calculated for 2000 m/s K atoms.

Parameter	Lens A_2	Lens B
Cylinder radius (R)	0.765 mm	6.350 mm
Cylinder edge to symmetry plane (a)	0.893 mm	1.960 mm
Electrode voltage (V)	−3.0 kV	± 6.0 kV
Paraxial focal length (f)	−6.1 km	−21.7 km

To cause uniform deflection over the height of our atom beam we orient the cylinders perpendicular to the atom beam velocity and normal to the plane of our atom interferometer (parallel to $\hat{y}$ in Fig. 1). In this orientation the electrodes can deflect atoms by 50 nm, which results in a π phase shift because we use 100-nm-period gratings for our atom interferometer. For comparison, several experiments [41–43] have deflected atoms by much larger distances (over 100 μm) with electrodes parallel to atom velocity. The Arndt group [9,44] used a gap between the curved ends of two custom-shaped electrodes to deflect molecules by several microns. However, unlike our lenses, the electrodes used in [9,41–44] cause nonuniform deflection over the height of the beam.

Diagrams of electrodes in this geometry and calculations of the associated atom wave phase shifts have been presented before [10,23,45–47]. However, here we use the idea of using an atom interferometer to characterize these electrodes as lenses with focal lengths in order to improve the analysis of measurements made with phase choppers.

Two copies of Lens A are installed in our atom interferometer as phase choppers. The first example of Lens A is located midway between the first two gratings. We refer to it as Lens A_1. The second one is located between the second and third gratings, where the outline of a lens in Fig. 1 is drawn. We refer to this one as Lens A_2. Lens B was built with a larger gap and larger cylinders as an interaction region for measurements of atomic polarizability. Lens B is located just in front of the second grating. We need both the velocity measurements from the phase choppers (Lens A_1 and A_2), as well as phase-shift measurements from Lens B in order to measure atomic polarizabilities.

IV. FRINGE SIMULATIONS

In this paper we introduce the idea that electrostatic magnification can compensate for geometric magnification in atom interferometers. To explain how this compensation works in more detail, we use simulations in this section to first discuss geometric magnification.

To visualize how fringes are formed in an extended region, we present simulations made with Gaussian-Schell model (GSM) beams. In brief, a GSM beam is a mathematical ensemble of Gaussian beams with parameters for beam width

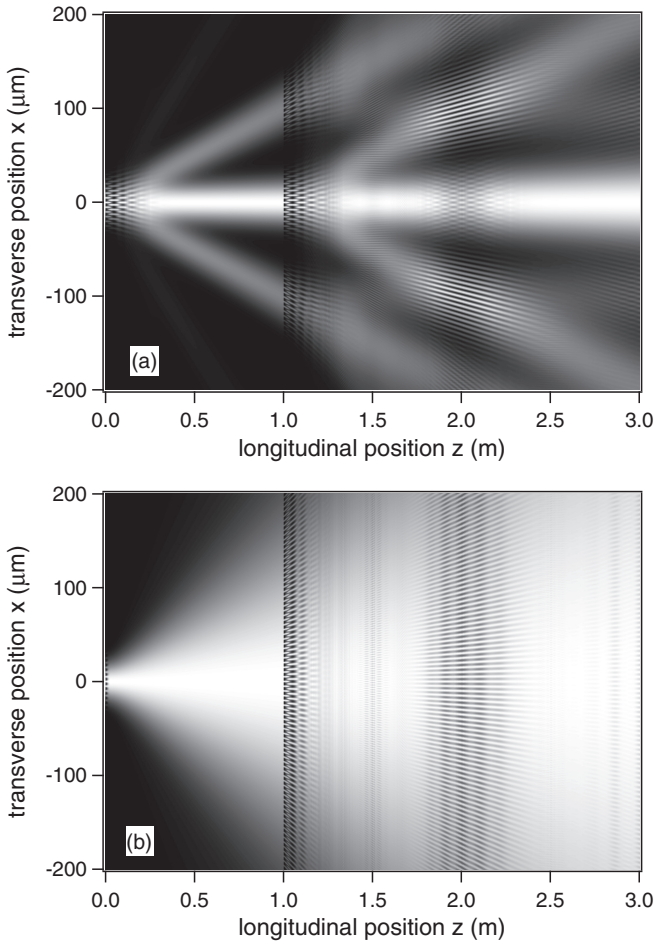

FIG. 2. Interference fringes formed after two gratings using a GSM beam simulation [48]. The probability density $|\Psi|^2$ is plotted on a gray scale in the 0.4-mm × 3-m region. Transmission gratings are located at $z = 0$ m and $z = 1$ m. The only difference between (a) and (b) is the transverse coherence of the GSM beam. In (a) fringes are formed in two distinct zones. In (b) the coherence length is shorter than the grating period, so the fringes appear to fan out in a range of directions, justifying the idea of geometric magnification (M_{geom}) defined in the text. $\hat{y}$ points out of the page.

and transverse coherence length [48–52]. Figure 2 shows the probability density for GSM beams as they propagate through two diffraction gratings located at $z = 0$ and $z = 1$ m. Table II lists the parameters used in each simulation. The key idea is that only mutually coherent portions of the diffracted GSM beam components interfere. Correlations between position and momentum of the beam components can then make interference fringes shift and spread out as a function of longitudinal position z.

TABLE II. Gaussian-Schell model beam parameters (at $z = 0$ m) used for the simulations shown in Fig. 2. These parameters were selected to illustrate how fringes patterns are affected by the transverse coherence length of the incident beam. For comparison, parameters that represent our experiment are also tabulated.

Parameter	Fig. 3(a)	Fig. 3(b)	Experiment
de Broglie wavelength	500 pm	500 pm	5 pm
Grating period	5 μm	5 μm	100 nm
Coherence length	25 μm	2.5 μm	50 nm
Beam width	30 μm	30 μm	30 μm
Velocity ratio (v_0/σ_v)	22	22	22

Local structures in the fringe period, phase, and contrast relate to our experimental signals in subtle ways, which is why the simulations are helpful. In the experiment, we average over much of this structure by using the third nanograting to moiré filter the fringes. The signal thus comes from the ensemble of transmitted atoms that strike our 100-μm-wide detector.

Figure 2(a) shows resolved diffraction, which occurs when a collimated beam has a transverse coherence length larger than the grating period. Interference fringes are then found in two distinct regions, as suggested by the rays that depict two symmetric Mach-Zehnder interferometers in Fig. 1. Fringes in these separate regions are in phase at $z = 2$ m but they shift away from each other (and become out of phase) as z increases. Thus, as the third grating is translated in the z direction, moiré filtering can lead to reductions and revivals in contrast as a function of ΔL, the difference between grating separations (see Fig. 1):

$$\Delta L = L_2 - L_1. \tag{5}$$

Figure 2(b) shows a simulation more representative of our experiments, in which the beam's initial transverse coherence length is slightly smaller than the grating period. Hence, diffraction is poorly resolved and the fringes diverge in a several directions. The way the fringe period changes with z can be described by geometric magnification:

$$M_{\text{geom}} = \frac{\Delta L + 2L_1}{2L_1}. \tag{6}$$

The fringe period is $d_f = M_{\text{geom}} d_g$, where d_g is the grating period. This geometric magnification occurs without a lens. It is a concept also found in studies of point-projection microscopy, the Lau effect [53], and Talbot-Lau interferometry [54,55]. Figures 2(a) and 2(b) both include an average over de Broglie wavelengths (i.e., atomic velocities) with a distribution typical of what we have in experiments, and still the geometric magnification is visible.

For a more nuanced discussion, the local pitch and orientation of the fringes depends on the momenta of the interfering wave components. Any two running waves with precise wave vectors $\mathbf{k_1}$ and $\mathbf{k_2}$ make standing wave interference fringes with a wave vector $\mathbf{k_f} = \mathbf{k_1} - \mathbf{k_2}$. However, even monochromatic Gaussian and GSM beams contain *distributions* of transverse momenta and thus make fringes with a range of pitches so that different $\mathbf{k_f}$ can be observed in different locations. For collimated beams, fringes follow lines parallel to $\overline{\mathbf{p}} = \hbar(\mathbf{k_1} + \mathbf{k_2})/2$. This is related to the the so-called *separation phase* that was named by Dimopoulos *et al.* in [56] to describe how fringes shift as atomic wave function components propagate through one another in a laboratory frame of reference. GSM beams from a small aperture make fringes that follow hyperbolae in the x-z plane. GSM beams from wider apertures make interference visible over a more limited range in z, where fringe patterns from different parts of the source still overlap in phase, as in Talbot-Lau interferometers [22]. Thus, Eq. (6) is approximate, but works well enough to describe how the

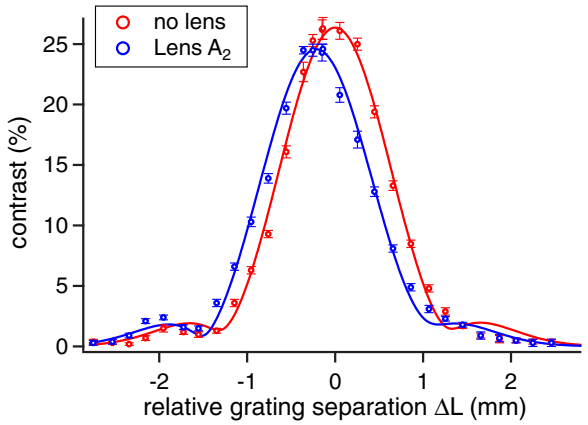

FIG. 3. (Color online) Contrast versus ΔL measured with and without a lens. The contrast envelope shifts in position by -205 ± 10 μm due to fringe magnification caused by the lens.

fringes diverge in our experiments. GSM beam simulations such as Fig. 2(b), with both transverse and longitudinal velocity distributions included in the simulation, help to justify this claim.

V. USING CONTRAST TO MEASURE f

In the first experiments, we scanned the second grating in the z direction to change ΔL. Figure 3 shows contrast data as a function of ΔL with and without Lens A_2 using a potassium atom beam with $v_0 \approx 2000$ m/s. The data exhibit peaks approximately 1.5 mm wide (FWHM in ΔL). There are also faint hints of contrast revivals at $\Delta L \approx \pm 2$ mm. Importantly, the lens causes the contrast to peak at a new location shifted by $\Delta L = -205 \pm 10$ μm. To interpret this shift as a measure of the focal length f, we use the idea that fringe magnification due to the electrostatic lens (M_{lens}) can compensate for geometric magnification (M_{geom}).

In optics parlance, the original fringes (with no lens) are a virtual object, located a distance $|o| \approx 33$ cm downstream of the lens. The weak diverging lens forms a real image of the fringes at a new location, a slightly greater distance i after the lens. The image has a transverse magnification $M_T = -i/o$, and these quantities are related to the focal length f by the imaging equation ($i^{-1} + o^{-1} = f^{-1}$). We use the convention that o is negative for a virtual object, i is positive for a real image, and f is negative for a diverging lens, as found in several optics texts [57,58].

Since the fringes are an extended object, we consider o to specify particular points within the object (in a plane with a given z). The image on the nanograting is therefore an image of that part of the object that was located upstream by a distance $i - |o| = |o^2/f|$, to first order in o/f. That part of the object had a smaller fringe period due to geometric magnification; hence, the object period was $d_o = d_g(2L_1 - |o^2/f|)/(2L_1)$. However, the image is magnified by the lens. Thus, without moving the nanogratings from a position where $\Delta L = 0$, the image has fringe period:

$$d_i = d_g\left(\frac{2L_1 - |o^2/f|}{2L_1}\right)\left(\frac{o + o^2/f}{o}\right). \tag{7}$$

The first factor in parentheses accounts for the ratio of object period to grating period (d_o/d_g) and the second factor in parentheses comes from the transverse magnification (M_T) by the lens. Hence, the lens causes fringes at $\Delta L = 0$ to be magnified, to first order in o/f, by

$$M_{\text{lens}} = 1 + \frac{o}{f}\left[1 + \frac{o}{2L_1}\right]. \tag{8}$$

M_{lens} is our theoretical prediction for how the period of the fringes on the third nanograting will change due to adding a lens. This is, of course, different than the standard definition of transverse magnification ($M_T = -i/o$) because M_T describes the ratio of the fringe period at the object location (with no lens) to the fringe period at the image location (with a lens). Even a magnification of $M_{\text{lens}} = 1.0005$ significantly reduces fringe contrast in our experiments because our detector is 1000 grating periods wide.

To deduce the focal length f of the lens, we measured the ΔL that maximizes contrast. We assume contrast peaks when the combined magnification $M_{\text{lens}}M_{\text{geom}}$ equals unity. Thus,

$$f = -\frac{2L_1 o + o^2}{\Delta L}. \tag{9}$$

Using our experimental parameters of $L_1 = 0.94$ m, $o = -0.33$ m, and $\Delta L = -0.205$ mm, we measured a focal length of $f = -2.5 \pm 0.13$ km for Lens A_2. As we discuss in the next sections, this is a nonparaxial focal length, which we refer to as the radius of curvature R_c.

It is noteworthy that we measured such a large focal length while sampling only a 100-μm-wide portion of a lens. With ordinary light optics this would be nearly impossible, because the wavelength of visible light is 100 000 times longer than the 5-pm atom waves used here. Hence, diffraction from the beam stops would obscure any change in beam properties caused by such a weak lens. In essence, we have monitored changes in collimation angle that are smaller than 5×10^{-8} rad, while diffraction of visible light from a 100-μm lens aperture would cause divergence on the order of 5×10^{-3} rad.

VI. USING PHASE TO MEASURE f

In a separate experiment to study focal lengths, we translated the lens in the x direction, perpendicular to the atom beam, and measured the differential phase shifts shown in Fig. 4. Since both interferometer arms go through the lens, we are using our apparatus as a shearing interferometer [53]. If the phase induced by the lens is denoted by $\Phi(x)$ for any single path through the lens, then the observed differential phase shift ϕ for an interferometer with paths separated by a distance s in the x direction is

$$\phi(x) = \Phi(x + s) - \Phi(x). \tag{10}$$

By measuring the fringe phase shift $\phi(x)$ as a function of lens position x, we mapped the derivative of $\Phi(x)$ as is typical for a shearing interferometer:

$$\phi(x) \approx \frac{d\Phi(x)}{dx} \cdot s. \tag{11}$$

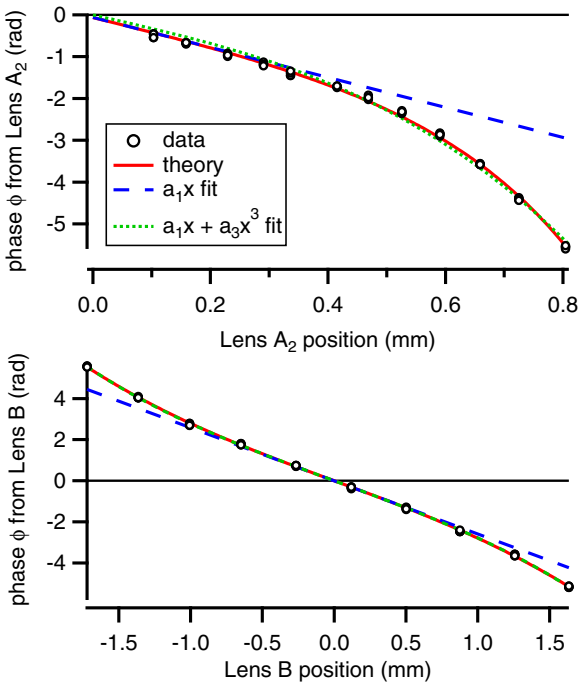

FIG. 4. (Color online) Atom interferometer differential phase-shift data. Graphs show measured values and theory for Lens A_2 (top) and Lens B (bottom). Differences from the linear fit shows deviation from an ideal thin lens. Error bars are smaller than the data symbols.

Therefore, a constant slope in $\phi(x)$ indicates a quadratic phase factor in $\Phi(x)$, as expected for a lens. Furthermore, nonlinearity in $\phi(x)$ indicates spherical aberration.

We use the slope $\Delta\phi/\Delta x$ locally to find the focal length f using a relationship derived for spherical waves,

$$f = k_g L\left(\frac{\Delta\phi}{\Delta x}\right)^{-1}, \tag{12}$$

where $k_g = 2\pi/d_g$ is the grating wave number ($d_g = 100$ nm), and for Lens A_2, $L = -o = 0.33$ m. The observed $\Delta\phi/\Delta x = -3.6$ rad/mm near the ground plane, so the paraxial focal length is -5.8 ± 0.3 km.

To describe spherical aberration, we also report how the focal length gets shorter as we use the lens farther away from its optical axis. At $x = 600$ μm, for example, the slope $\Delta\phi/\Delta x$ increases to -8.8 rad/mm for Lens A_2 and the R_c is -2.4 km. This is consistent with the focal length measurement for lens A_2 that we obtained in Sec. V because $x = 600 \pm 50$ μm was the position of Lens A_2 for contrast measurements in Fig. 3.

We also measured f for Lens B. Data in Fig. 4(b) shows $\Delta\phi/\Delta x = -2.6$ rad/mm near the optical axis. Thus, the paraxial focal length for Lens B is $f = -20.0 \pm 1.0$ km. With Lens B off axis by $x = 1.15$ mm, we observed $\Delta\phi/\Delta x = -3.4$ rad/mm and thus infer that R_c is -15.3 ± 0.8 km.

Spherical aberration can also be quantified by fitting $\phi(x)$ with a polynomial $a_1(x/b) + a_3(x/b)^3$. The best-fit parameter a_3 for Lens A_2 gives $W_{SA4} = a_3/(8\pi s) = 32 \pm 3$ waves and for Lens B gives $W_{SA4} = 130 \pm 27$, where W_{SA4} is the fourth-order spherical abberation coefficient as discussed in the next section.

VII. CALCULATED f AND ABERRATIONS

In the previous two sections we presented atom optical shop testing experiments that served to measure the focal length and spherical aberrations of a lens for atoms. Next, we calculate the focal length and spherical aberration coefficients for our atom lenses to check the measurement results.

The atom wave phase induced by our lens [10,23,45–47] is

$$\Phi(x) = \frac{4\pi\alpha V^2}{\hbar v}\ln^{-2}\left(\frac{a+R+b}{a+R-b}\right)\frac{b}{b^2-x^2}, \tag{13}$$

where α is the atomic polarizability, V is the electrode voltage with respect to the ground plane, v is the atom beam velocity, x is the beam position relative to the optical axis, and $b = a\sqrt{1+2R/a}$ is related to the geometry of the electrodes (see Table I), where R is the radius of the cylindrical electrode and a is the electrode spacing for Lens A (or half the spacing for Lens B).

To calculate the focal length and spherical aberration coefficients of our lenses, we first find the surface of constant phase z, or wave front, induced by the lens by evaluating $\Phi = -k_{dB}z$,

$$z(x) = -\frac{\alpha(V/c)^2}{mv^2}\frac{b}{1-(x/b)^2}, \tag{14}$$

where $c = b(4\pi)^{-1/2}\ln[(a+R+b)/(a+R-b)]$ has units of length and is comparable to the gap size in our experiments ($c = 1.17$ mm for Lens A and $c = 2.32$ mm for Lens B). Written this way, $z(x)$ depends on the ratio of the potential energy $U = -\alpha E^2/2$ to the kinetic energy $K = mv^2/2$. This relation is expected since the index of refraction for atom waves due to the electric field is $n = (1-U/K)^{1/2}$ [59]; hence, $n-1$ depends to first order linearly on the small parameter (U/K). Therefore, we introduce a dimensionless parameter $g = \alpha(V/c)^2/(mv^2)$ for what follows. In our experiments $g \approx 10^{-7}$, which explains why the focal lengths are so long for our electrostatic lenses for atoms.

The radius of curvature, R_c of the isophase surface z can be found from a local circle fit to Eq. (14) (the so-called osculating circle):

$$R_c = -\frac{b}{2g}\frac{\{[1-(x/b)^2]^4 - 4g^2(x/b)^2\}^{3/2}}{[1+3(x/b)^2][1-(x/b)^2]^3}. \tag{15}$$

Equation (15) also shows how the radius of curvature R_c depends on the distance from the optical axis x (spherical aberration) and the de Broglie wavelength λ_{dB} since g depends on v^{-2} (chromatic aberration). At $x = 0$, i.e., on the optical axis, the focal length is equal to R_c; hence,

$$f = -\frac{b}{2g}. \tag{16}$$

For a 2000 m/s potassium atom beam, we calculate $f = -6.1$ km for Lens A_2 and $f = -21.7$ km for Lens B. These calculations are in agreement with the focal length measurements. For Lens A_2 at $x = 600$ μm, $R_c = -2.3$ km. This calculation is also consistent with the measurements of R_c in Sec. VI.

Next, we study $z(x)/\lambda_{db} = W_A$, known as the aberrated wave front, which we have expressed in units of waves. We

proceed by expanding W_A in a Taylor series as is done in light optics [60,61]:

$$W_A = -\frac{bg}{\lambda_{dB}}\left[1 + \left(\frac{x}{b}\right)^2 + \left(\frac{x}{b}\right)^4 + \cdots\right]. \quad (17)$$

The zeroth-order term in x/b, the first term in brackets, is position independent and corresponds to an optical flat with no optical power. The second-order term is the focusing term. It corresponds to an ideal lens with a focal length $f = -b/(2g)$, same as the paraxial focal length in Eq. (16).

To determine the spherical aberration, we first calculate the wave-front error $W = W_A - W_R$, where W_R is an unaberrated reference spherical wave front with a radius of curvature equal to the paraxial focal length. For our lenses, the focal length is 10^7 times greater than the lens aperture, so the difference between a spherical reference wave front and a parabolic wave front is negligible. Therefore, $W \approx W_A$ for higher-order terms in x/b.

Terms that are fourth order and higher in x/b describe the different order spherical aberrations. For our electrostatic lenses, the wave-front spherical aberration coefficients are the same for all orders of spherical aberration. We therefore refer to the coefficients as W_{SA}. For our lenses,

$$W_{SA} = -\frac{bg}{\lambda_{dB}}. \quad (18)$$

For Lens A_2 and a 2000 m/s potassium atom beam, we compute $W_{SA} = -35$ waves. Similarly, for Lens B we compute $W_{SA} = -130$ waves. This indicates that 1.12 mm from the optical axis for Lens B there is only a 1/4 de Broglie wave (1 pm) deviation between W_A and W_R. These calculations are in agreement with the measurements of the fourth-order spherical aberration coefficient W_{SA4} for Lens A_2 and Lens B in Sec. VI.

There is also axial chromatic aberration and spherochromatism in our electrostatic lenses [60] because the focal length depends on λ_{dB}^{-2} and the spherical aberration coefficients are proportional to λ_{dB}^{-3}.

VIII. APPLICATION FOR VELOCITY MEASUREMENTS

Now we return to the problem of explaining how defocusing by phase choppers (Lens A_1 and Lens A_2) affects the accuracy of our atom beam velocity measurements. Although we have made mean velocity measurements using phase choppers with 0.05% statistical precision [46] (and again in Fig. 5), a systematic error of approximately 0.1% can be attributed to defocusing. Furthermore, this error changes with ΔL. We learned to recognize and fix this problem by studying how electric-field gradients act as lenses for atom waves.

Holmgren *et al.* [23] described how phase choppers are used to measure the velocity of atom beams. In brief, as mentioned in Sec. I, phase choppers are analogous to mechanical choppers. However, fringe contrast, rather than beam flux, is modulated as a function of chopping frequency, ν. We analyze $C(\nu)$ data to measure the mean velocity and the velocity spread of our atom beam, as shown in Fig. 5. The mean velocity determines the frequencies at which the contrast revivals occur, and the velocity spread affects how the contrast revivals decay.

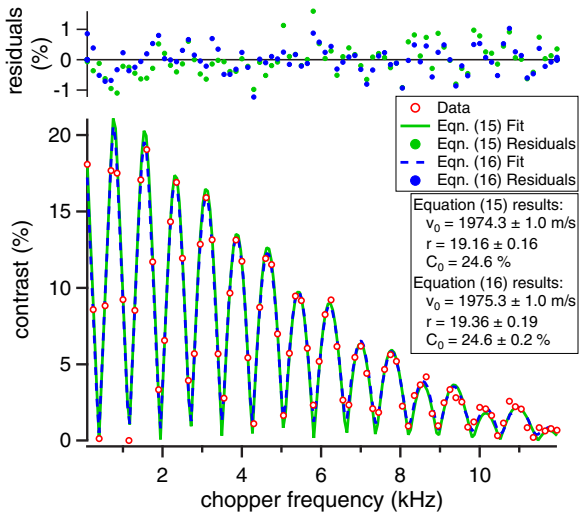

FIG. 5. (Color online) Contrast data versus chopping frequency $C(\nu)$ analyzed with Eqs. (20) and (19). The best-fit parameters for the most probable velocity and velocity ratio (v_0 and r) are discussed in the text.

Equation (1) of Ref. [23] modeled the contrast and phase of the interference fringes by

$$C(\nu)e^{i\phi(\nu)} = C_0 e^{i\phi_0}\nu \int_{t=0}^{1/\nu}\int_{v=0}^{\infty} P(v) \times e^{i[\phi_1(v,t)+\phi_2(v,t+\ell/v)]}dvdt, \quad (19)$$

where ϕ_1 and ϕ_2 were the v-dependent (but x-independent) phase shifts due to choppers A_1 and A_2, and $P(v)$ is the probability distribution for velocity. We use a Gaussian $P(v) = (2\pi\sigma^2)^{-1/2}\exp[-(v-v_0)^2/(2\sigma_v^2)]$ and keep both v_0 and the ratio $r = v_0/\sigma_v$ as free parameters when comparing Eq. (19) to $C(\nu)$ data.

Now we use our analysis of lenses inside an atom interferometer to develop an improved model that includes the thickness of the atom beam and its angular spread by explicitly averaging over all detected trajectories. We do this by integrating over all transverse positions in the two collimating slits (having widths w_1 and w_2, respectively). We also include the transverse coherence length of the atom beam, the symmetric pairs of interferometers sketched in Fig. 1, and the finite size of the atom beam detector. We thus replace Eq. (19) with

$$C(\nu)e^{i\phi(\nu)} = C_0 e^{i\phi_0}\frac{1}{2}\sum_{j=-1,1}\int_{x_1=-w_1/2}^{+w_1/2}\int_{x_2=-w_2/2}^{+w_2/2} \times \nu\int_{t=0}^{1/\nu}\int_{v=0}^{\infty} P(v)D_j(x_1,x_2,v) \times e^{i[\phi_{1j}(x_1,x_2,v,t)+\phi_{2j}(x_1,x_2,v,t+\ell/v)]} \times e^{i\phi_{\mathrm{sep},j}(x_1,x_2,v,\Delta L)}C_{\mathrm{env}}(\Delta L,t) \times e^{i\phi_{\mathrm{sag}}(v)}dvdtdx_1dx_2, \quad (20)$$

where C_0 is the reference contrast observed when $\Delta L = 0$ and the electrodes are grounded. The index j identifies different interferometers that are formed by different pairs

of diffraction orders (two such interferometers are sketched in Fig. 1). $D_j(x_1,x_2,v)$ describes the probability that atoms hit the detector after passing through positions x_1 and x_2 in the two collimating slits and diffracting in the directions given by j and v.

The terms ϕ_{ij} in Eq. (20) with $i \in (1,2)$ represent the differential phase imparted by chopper i to atoms that fly by with wave-function components at transverse positions x_{ij} and $x_{ij}+s$. Once these positions are determined, then the phases ϕ_{ij} can be calculated using Eq. (13). These positions depend on x_1, x_2, v, and j; therefore, ϕ_{ij} should be evaluated inside the integrals and the sum in Eq. (20). The terms ϕ_{ij} describe the phase curvature and thus the magnification M_{lens} caused by the phase choppers.

The terms $\phi_{\text{sep},j}(x_1,x_2,v,\Delta L)$ and $C_{\text{env}}(\Delta L,t)$ depend explicitly on ΔL. This is new, because Eq. (19) had no terms that depend on ΔL. The separation phase $\phi_{\text{sep},j}(x_1,x_2,v,\Delta L)$ describes how the fringes change in phase locally as wave-function components propagate through one another to planes with a different ΔL. This is the origin of geometric magnification M_{geom}. The term $C_{\text{env}}(\Delta L,t)$ represents an additional contrast reduction due to the transverse coherence length of the wave packets. $C_{\text{env}}(\Delta L,t)$ depends on t because it shifts slightly when the phase choppers are turned on. We model the separation phase as

$$\phi_{\text{sep},j}(x_1,x_2,v,\Delta L) = k_g\left[\theta_{\text{inc}}(x_1,x_2) + \frac{j}{2}\frac{\lambda_{dB}}{d_g}\right]\Delta L, \tag{21}$$

where θ_{inc} is the angle of incidence on the first grating. The sum $[\theta_{\text{inc}}(x_1,x_2) + (j/2)(\lambda_{dB}/d_g)]$ represents the angle of the fringe maxima in the x-z plane (see Fig. 2 in Sec. IV). We model the contrast envelope due to transverse coherence length as

$$C_{\text{env}}(\Delta L,t) = e^{-\frac{1}{2}(\frac{\Delta L}{L_1}\frac{w_s}{d_g})^2}, \tag{22}$$

where w_s is the size of an effective collimating slit, and d_g is the grating period. This is based on the van Cittert Zernike theorem and an assumption that the transverse coherence is well described by incoherent illumination of a Gaussian-weighted first collimating slit with Gaussian FWHM given by $w_s = w_1$. We have also modeled C_{env} with GSM beams (e.g., in Sec. IV).

With some approximations that we describe, the integral over $e^{i\phi_{\text{sep}}}$ and C_{env} across the width of the detected atom beam produces contrast patterns that depend on ΔL in a way we can write analytically

$$\frac{C}{C_0} = \text{sinc}\left(\Delta k\frac{w_d}{2}\right)e^{-\frac{1}{2}(\frac{\Delta L}{L_1}\frac{w_s}{d_g})^2}, \tag{23}$$

where Δk is the difference between the grating wave number $k_g = 2\pi/d_g$ and the fringe wave number and w_d is the width of the detector. We can explicitly write Δk in terms of fringe magnification as

$$\Delta k = k_g(M_{\text{geom}}M_{\text{lens}} - 1). \tag{24}$$

The sinc term [defined as $\text{sinc}(x) = \sin(x)/x$] is found as a result of making the approximation that the detector is uniformly illuminated. Although Eq. (23) reproduces the theory functions shown in Fig. 3 fairly well, the full description in Eq. (20) is more complete because it takes into account how the detected beam flux as a function of position on the detector depends on the sizes and locations of the collimating slits. Equation (20) also includes the integral over velocity, which further reduces the contrast by the factor $e^{-\frac{1}{2}(2\phi_0/r)^2}$, where ϕ_0 is the phase shift caused by the lens for atoms with velocity v_0. This factor amounts to $C/C_0 = 0.95$ for the data shown in Fig. 3, which is consistent with $\phi_0 = \pi$ (when the chopper is on) and $r = v_0/\sigma_v = 20$. For completeness, we note that the contrast as a function of ΔL for atom beam interferometers has also been discussed in [62,63] with different assumptions such as Bragg diffraction.

The Sagnac phase is $\phi_{\text{sag}} = 4\pi L_1^2\Omega_y/(vd_g)$, where Ω_y is the vertical component of the laboratory rotation rate and d_g is the grating period. In our laboratory the Sagnac phase is 2.4 rad for 2000 m/s atoms due to Earth's rotation rate. The velocity dependence of the Sagnac phase can change the resulting best fit v_0 in our experiments by 0.05%. Similar sensitivity to the Sagnac phase was noted in [10].

Using Eq. (19) as opposed to Eq. (20) to make a least-squares fit to data in Fig. 5 results in slightly different parameter values for v_0 and r. The values of v_0 using the two theoretical models are different by about 0.2% for atom beams with $v_0 \approx$ 1000 m/s, and the model-dependant differences in best fit v_0 become smaller for higher-velocity atom beams. To investigate which analysis is more accurate, we were motivated to test other predictions of focusing behavior, such as $C(\Delta L)$ data shown in Fig. 3 and $\phi(x)$ data shown in Fig. 4 as further evidence that Eq. (20) is indeed more accurate than Eq. (19).

Next, we examine model-dependent differences in the best-fit parameters v_0 and r as a function of ΔL. We used Eq. (20) to simulate $C(v)$ spectra with particular v_0 and r given as input parameters. Then, we used the simpler model described by Eq. (19) to find the best-fit parameters $\tilde{v_0}$ and $\tilde{r}$ that minimize the sum of the squared errors when analyzing the simulated data. The differences $\tilde{v_0} - v_0$ and $\tilde{r} - r$ depend on ΔL, as shown in Fig. 6. This is significant because ΔL was not even considered as a parameter in earlier work on phase choppers [23,46,47], but Fig. 6 now shows that it is important.

Most trends in Fig. 6 can be explained by fringe magnification. For example, reduction in contrast due to focusing can be misinterpreted as a larger spread in velocity. In particular, if $\Delta L > 0$, then focusing reduces the contrast, so Eq. (19) makes a best fit $\tilde{r}$ too low. Conversely, when $\Delta L < 0$ choppers can increase contrast, as we saw in Fig. 3, and as a consequence the best fit $\tilde{r}$ is too large. Hence, the combined influence of ϕ_{ij} and ϕ_{sep} (electrostatic and geometric magnification) causes errors in $\tilde{r}$ that can be anticorrelated with ΔL, as seen in Fig. 6. Velocity-dependent contrast suppression and velocity-dependent detection included in Eq. (20) but not Eq. (19) also influence errors in $\tilde{r}$.

Trends in $\tilde{v_0}$ are similarly subtle but can also be explained, for the most part, in terms of magnification. One reason for an error in $\tilde{v_0}$ is that slow atoms, with a larger diffraction angle, preferentially miss the detector. This is described by $D_j(x_1,x_2,v)$. Just as importantly, when the slower atoms in the ensemble contribute to the signal with low contrast as a result of a mechanism not adequately described by Eq. (19), then

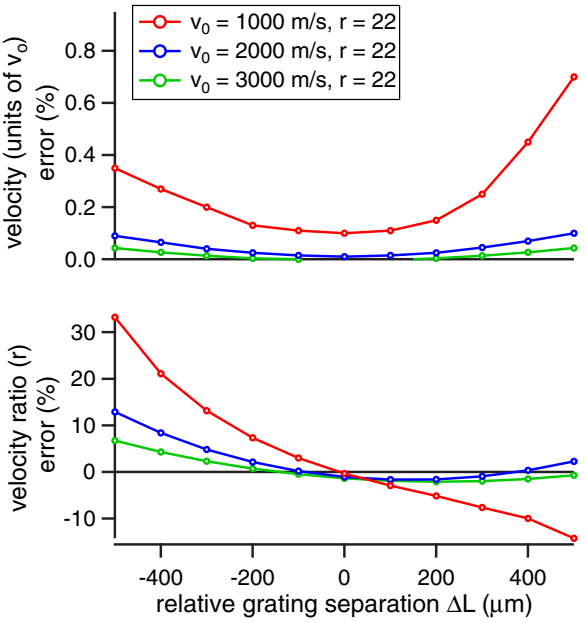

FIG. 6. (Color online) Error in best-fit velocity as a function of ΔL using Eq. (19) to fit simulated data generated with the more complete model described by Eq. (20). The velocity error is $(\tilde{v}_0 - v_0)/v_0$ and the error in velocity ratio is $(\tilde{r} - r)/r$ as described in the text.

there will be a bias towards faster $\tilde{v}_0$. Preferential contrast loss for slow atoms is caused, for example, by geometric magnification (ϕ_{sep}) simply because of the larger diffraction angles. Also, electrostatic magnification (ϕ_{ij}) generally produces velocity-dependent contrast loss due to chromatic aberrations. However, when ΔL is slightly negative, the signal can be biased towards slower atoms because electrostatic magnification then compensates for geometric magnification preferentially for the slow atoms.

We have documented our effort to validate the model in Eq. (20) with auxiliary tests, e.g., in Figs. 3 and 4, so we are convinced that Eq. (20) is an improvement over Eq. (19). Furthermore, in case there are still additional position- and velocity-dependent phases that we have not yet discovered that make an impact on our analysis, we can offer a strategy to minimize errors in measurements of v_0 and r by operating at a ΔL, where errors are minimum. We note there are minima in the absolute value of $\tilde{v}_0$ error and $\tilde{r}$ error in Fig. 6 when $\Delta L = -100$ μm. The reason for a minimum error is that at this ΔL the contrast change due to the phase choppers is very small for atoms with v_0 (e.g., this is where the two contrast curves intersect in Fig. 3). Therefore, we recommend operating future phase-chopper experiments with ΔL chosen so the observed contrast is not affected by the phase choppers. Then, even a simpler model that is missing some contrast-reducing mechanisms [e.g., Eq. (19)] still produces a smaller error in $\tilde{v}_0$ and $\tilde{r}$ than it would if $\Delta L = 0$.

IX. DISCUSSION

In summary, de Broglie wave-front curvature induced by phase choppers influences measurements of atom beam velocity in an atom interferometer. Electrostatic phase choppers inevitably act like lenses that magnify atom interference fringes, and thus modify the observed fringe contrast. Measurements of contrast as a function of nanograting location, $C(\Delta L)$, showed how electrostatic magnification of atom interference fringes can compensate for geometric magnification. This observation explained systematic shifts in measurements of atomic beam velocity v_0 and velocity ratio r made with phase choppers. Then, an improved model of $C(\nu)$ was developed to reduce these systematic errors. Systematic corrections were shown to depend on ΔL, a parameter that had not previously been considered in the analysis of phase choppers.

Measurements of phase shifts $\phi(x)$ induced by a lens were used as an independent measurement of the focal length of atom lenses. The focal length was measured with less than 5% uncertainty, even though the values of f that we studied were quite large (ranging from -2.5 to -21.7 km). We also used $\phi(x)$ to measure spherical aberration. Calculations of wave-front curvature induced by electrostatic lenses were used an an additional method to determine the focal length f. The calculations were consistent with measurements of wave-front radius of curvature using contrast and phase measurements and were then used in the improved model of $C(\nu)$.

The goal of this improved model of phase-chopper $C(\nu)$ spectra is to support future measurements of atomic polarizability. For this application we recommend monitoring ΔL using contrast measurements and incorporating uncertainty in ΔL into the error budget for resulting measurements of atomic velocities, velocity ratios, and ultimately polarizabilities. Additional modifications to Eq. (20) may be explored, such as diffraction phases induced by the gratings themselves [64], but we suspect that diffraction phases in particular can be incorporated simply by using the contrast peak to redefine where $\Delta L = 0$. Thus, we recommend measuring ΔL with respect to the contrast peak and then selecting a ΔL that makes the phase choppers cause minimal changes in contrast.

To give a broader perspective, electron and optical interferometers routinely use lenses to intensify, magnify, and focus fringes. Neutron optics experiments [65] have also begun to include magnetic hexapole [66] or solid-state lenses [67,68] as tools to manage neutron beams. Therefore, given the many examples of atom lenses discussed in the literature [24–40], we expect that several new opportunities may result from using lenses for atoms in conjunction with an atom interferometer. In this paper we used this nexus to develop atom optical shop testing, in analogy to ordinary optical shop testing [57,58,60,61,69,70]. We also explored systematic corrections to precision measurements that arise when de Broglie wave curvature is manipulated inside an atom interferometer.

The analogy of a lens in an interferometer may be extended to ultracold atom interferometers operated in traps. However, in traps the parameter $g = U/K$ is often larger than 1 and the interaction time with the trap potential can be many times the inverse trap frequency. In comparison, for experiments presented here $g \approx 10^{-7}$, the fly-by time was a few μs, and the resulting the displacement of atoms within the lens was negligible compared to the atom beam width or even its transverse coherence length. Thus, the electric-field gradients we studied are like weak, diverging, cylindrical, thin lenses for atoms, whereas traps are more similar to waveguides for atoms [21,71,72].

Finally, we speculate on some additional uses for lenses in atom interferometers. Schemes may be developed to magnify atom interference fringes to make them easier to image. We also propose that lenses can compensate for gratings that have the wrong period. For example, if the nanogratings in a hybrid KD-TLI interferometer [73] are imperfectly matched with the laser grating period, then atom lenses may improve the fringe contrast. Spherical aberration can compensate for grating chirp. Strong positive lenses can focus beams inside atom interferometers to increase flux and reduce beam widths. Atom optical shop testing with an atom interferometer could also validate aberration mitigation techniques such as those proposed in [74,75].

ACKNOWLEDGMENTS

This work is supported by NSF Grant No. 1306308 and a NIST PMG. R.T. and M.D.G. are grateful for NSF GRFP Grant No. DGE-1143953 for support. W.F.H. thanks the Arizona TRIF for additional support.

[1] T. Gustavson, A. Landragin, and M. Kasevich, Classical Quantum Gravity **17**, 2385 (2000).
[2] A. Peters, K. Y. Chung, and S. Chu, Metrologia **38**, 25 (2001).
[3] J. M. McGuirk, G. T. Foster, J. B. Fixler, M. J. Snadden, and M. A. Kasevich, Phys. Rev. A **65**, 033608 (2002).
[4] G. Lamporesi, A. Bertoldi, L. Cacciapuoti, M. Prevedelli, and G. M. Tino, Phys. Rev. Lett. **100**, 050801 (2008).
[5] J. Fixler, G. Foster, J. McGuirk, and M. Kasevich, Science **315**, 74 (2007).
[6] A. Wicht, J. M. Hensley, E. Sarajlic, and S. Chu, Phys. Scr. **T102**, 82 (2002).
[7] C. R. Ekstrom, J. Schmiedmayer, M. S. Chapman, T. D. Hammond, and D. E. Pritchard, Phys. Rev. A **51**, 3883 (1995).
[8] A. Miffre, M. Jacquey, M. Büchner, G. Trenec, and J. Vigue, Phys. Rev. A **73**, 011603 (2006).
[9] M. Berninger, A. Stefanov, S. Deachapunya, and M. Arndt, Phys. Rev. A **76**, 013607 (2007).
[10] W. F. Holmgren, M. C. Revelle, V. P. A. Lonij, and A. D. Cronin, Phys. Rev. A **81**, 053607 (2010).
[11] J. D. Perreault and A. D. Cronin, Phys. Rev. Lett. **95**, 133201 (2005).
[12] W. F. Holmgren, R. Trubko, I. Hromada, and A. D. Cronin, Phys. Rev. Lett. **109**, 243004 (2012).
[13] D. A. Kokorowski, A. D. Cronin, T. D. Roberts, and D. E. Pritchard, arXiv:quant-ph/0009044.
[14] K. Hornberger, S. Uttenthaler, B. Brezger, L. Hackermüller, M. Arndt, and A. Zeilinger, Phys. Rev. Lett. **90**, 160401 (2003).
[15] H. Uys, J. D. Perreault, and A. D. Cronin, Phys. Rev. Lett. **95**, 150403 (2005).
[16] L. Hackermüller, S. Uttenthaler, K. Hornberger, E. Reiger, B. Brezger, A. Zeilinger, and M. Arndt, Phys. Rev. Lett. **91**, 090408 (2003).
[17] K. Zeiske, G. Zinner, F. Riehle, and J. Helmcke, Appl. Phys. B **60**, 205 (1995).
[18] S. Yanagimachi, M. Kajiro, M. Machiya, and A. Morinaga, Phys. Rev. A **65**, 042104 (2002).
[19] S. Lepoutre, A. Gauguet, G. Trénec, M. Büchner, and J. Vigué, Phys. Rev. Lett. **109**, 120404 (2012).
[20] Edited by P. Berman, *Atom Interferometry* (Academic Press, San Diego, 1997).
[21] A. D. Cronin, J. Schmiedmayer, and D. E. Pritchard, Rev. Mod. Phys. **81**, 1051 (2009).
[22] K. Hornberger, S. Gerlich, P. Haslinger, S. Nimmrichter, and M. Arndt, Rev. Mod. Phys. **84**, 157 (2012).
[23] W. F. Holmgren, I. Hromada, C. E. Klauss, and A. D. Cronin, New J. Phys. **13**, 115007 (2011).
[24] W. G. Kaenders, F. Lison, I. Müller, A. Richter, R. Wynands, and D. Meschede, Phys. Rev. A **54**, 5067 (1996).
[25] A. Jardine, P. Fouquet, J. Ellis, and W. Allison, Rev. Sci. Instrum. **72**, 3834 (2001).
[26] R. Chaustowski, V. Leung, and K. Baldwin, App. Phys. B **86**, 491 (2006).
[27] W. Ketterle and D. Pritchard, App. Phys. B **54**, 403 (1992).
[28] J. P. Gordon, Phys. Rev. **99**, 1253 (1955).
[29] H.-R. Noh, K. Shimizu, and F. Shimizu, Phys. Rev. A **61**, 041601 (2000).
[30] J. G. Kalnins, J. M. Amini, and H. Gould, Phys. Rev. A **72**, 043406 (2005).
[31] O. Carnal, M. Sigel, T. Sleator, H. Takuma, and J. Mlynek, Phys. Rev. Lett. **67**, 3231 (1991).
[32] S. Rehbein, R. B. Doak, R. E. Grisenti, G. Schmahl, J. P. Toennies, and C. Wll, AIP Conf. Proc. **507**, 688 (2000).
[33] J. E. Bjorkholm, R. R. Freeman, A. Ashkin, and D. B. Pearson, Phys. Rev. Lett. **41**, 1361 (1978).
[34] Sleator, T. Pfau, V. Balykin, and J. Mlynek, App. Phys. B **54**, 375 (1992).
[35] J. McClelland, J. Opt. Soc. Am. B **12**, 1761 (1995).
[36] R. B. Doak, R. E. Grisenti, S. Rehbein, G. Schmahl, J. P. Toennies, and C. Wöll, Phys. Rev. Lett. **83**, 4229 (1999).
[37] M. Koch, S. Rehbin, G. Schmahl, T. Reisinger, G. Bracco, W. E. Ernst, and B. Holst, J. Microsc. **229**, 1 (2008).
[38] C. Bradley, W. Anderson, J. McClelland, and R. Celotta, Appl. Surf. Sci. **141**, 210 (1999).
[39] G. Timp, R. E. Behringer, D. M. Tennant, J. E. Cunningham, M. Prentiss, and K. K. Berggren, Phys. Rev. Lett. **69**, 1636 (1992).
[40] J. McClelland, R. Scholten, E. Palm, and R. Celotta, Science **262**, 877 (1993).
[41] W. D. Hall and J. C. Zorn, Phys. Rev. A **10**, 1141 (1974).
[42] H. L. Schwartz, T. M. Miller, and B. Bederson, Phys. Rev. A **10**, 1924 (1974).
[43] S. Schäfer and R. Schäfer, Phys. Rev. B **77**, 205211 (2008).
[44] A. Stefanov, M. Berninger, and M. Arndt, Meas. Sci. Technol. **19**, 055801 (2008).
[45] T. D. Roberts, A. D. Cronin, M. V. Tiberg, and D. E. Pritchard, Phys. Rev. Lett. **92**, 060405 (2004).
[46] W. F. Holmgren, Ph.D. thesis, University of Arizona, 2013.
[47] C. E. Klauss, B.S. thesis, University of Arizona, Tucson, 2011.
[48] B. McMorran and A. D. Cronin, Phys. Rev. A **78**, 013601 (2008).

[49] A. T. Friberg and R. J. Sudol, Opt. Commun. **41**, 383 (1982).
[50] A. T. Friberg and R. J. Sudol, J. Mod. Opt. **30**, 1075 (1983).
[51] F. Gori, G. Guattari, and C. Padovani, Opt. Commun. **64**, 491 (1987).
[52] B. McMorran and A. Cronin, arXiv:0804.1162.
[53] K. Patorski, Prog. Opt. **27**, 1 (1989).
[54] J. Clauser and M. Reinsch, App. Phys. B **54**, 380 (1992).
[55] B. Brezger, M. Arndt, and A. Zeilinger, J. Opt. B **5**, S82 (2003).
[56] S. Dimopoulos, P. W. Graham, J. M. Hogan, and M. A. Kasevich, Phys. Rev. D **78**, 042003 (2008).
[57] E. Hecht, *Optics* (Addison Wesley Longman, Boston, 1998).
[58] F. L. Pedrotti, *Introduction to Optics*, 3rd ed. (Pearson Education India, Noida, India, 2008).
[59] C. Adams, M. Sigel, and J. Mlynek, Phys. Rep. **240**, 143 (1994).
[60] J. E. Greivenkamp, *Field Guide to Geometrical Optics* (SPIE Press, Bellingham, WA, 2004).
[61] J. Sasián, *Introduction to Aberrations in Optical Imaging Systems* (Cambridge University Press, Cambridge, U.K., 2012).
[62] C. Champenois, M. Büchner, and J. Vigué, Eur. Phys. J. D **5**, 363 (1999).
[63] A. Miffre, M. Jacquey, M. Büchner, G. Trenec, and J. Vigue, Eur. Phys. J. D **33**, 99 (2005).
[64] J. D. Perreault and A. D. Cronin, Phys. Rev. A **73**, 033610 (2006).
[65] H. Rauch and S. A. Werner, *Neutron Interferometry: Lessons in Experimental Quantum Mechanics*, Vol. 12 (Oxford University Press, Oxford, U.K., 2000).
[66] T. Oku and H. Shimizu, Physica B **283**, 314 (2000).
[67] M. Kumakhov and V. Sharov, Nature (London) **357**, 390 (1992).
[68] H. Beguiristain, I. Anderson, C. Dewhurst, M. Piestrup, J. Cremer, and R. Pantell, Appl. Phys. Lett. **81**, 4290 (2002).
[69] Edited by D. Malacara, *Optical Shop Testing*, 3rd ed. (Wiley & Sons, Hoboken, NJ, 2007).
[70] E. P. Goodwin and J. C. Wyant, *Field Guide to Interferometric Optical Testing* (SPIE Press, Bellingham, Washington, 2006).
[71] P. Meystre, *Atom Optics* (Springer, Berlin, 2001), Vol. 33.
[72] R. Folman, P. Krüger, J. Schmiedmayer, J. Denschlag, and C. Henkel, Adv. At. Mol. Opt. Phys. **48**, 263 (2002).
[73] S. Gerlich, L. Hackermüller, K. Hornberger, A. Stibor, H. Ulbricht, M. Gring, F. Goldfarb, T. Savas, M. Müri, M. Mayor *et al.*, Nat. Phys. **3**, 711 (2007).
[74] D. Pritchard, *in Atomic Physics*, edited by C. Zorn and R. Lewis (AIP, New York, 1991), pp. 165–174.
[75] M. A. Efremov, P. V. Mironova, and W. P. Schleich, Phys. Rev. A **87**, 023604 (2013).